



Digging into the Interior of Hot Cores with ALMA (DIHCA). II. Exploring the Inner Binary (Multiple) System Embedded in G335 MM1 ALMA1

Fernando A. Olguin¹ , Patricio Sanhueza^{2,3} , Adam Ginsburg⁴ , Huei-Ru Vivien Chen¹ , Qizhou Zhang⁵ , Shanghuo Li⁶ , Xing Lu⁷ , and Takeshi Sakai⁸

¹ Institute of Astronomy and Department of Physics, National Tsing Hua University, Hsinchu 30013, Taiwan; folguin@phys.nthu.edu.tw

² National Astronomical Observatory of Japan, National Institutes of Natural Sciences, 2-21-1 Osawa, Mitaka, Tokyo 181-8588, Japan

³ Department of Astronomical Science, SOKENDAI (The Graduate University for Advanced Studies), 2-21-1 Osawa, Mitaka, Tokyo 181-8588, Japan

⁴ Department of Astronomy, University of Florida, P.O. Box 112055, Gainesville, FL, USA

⁵ Center for Astrophysics | Harvard & Smithsonian, 60 Garden Street, Cambridge, MA 02138, USA

⁶ Korea Astronomy and Space Science Institute, 776 Daedeokdae-ro, Yuseong-gu, Daejeon 34055, Republic of Korea

⁷ Shanghai Astronomical Observatory, Chinese Academy of Sciences, 80 Nandan Road, Shanghai 200030, People's Republic of China

⁸ Graduate School of Informatics and Engineering, The University of Electro-Communications, Chofu, Tokyo 182-8585, Japan

Received 2021 December 17; revised 2022 February 23; accepted 2022 March 7; published 2022 April 13

Abstract

We observed the high-mass protostellar core G335.579–0.272 ALMA1 at ~ 200 au ($0''.05$) resolution with the Atacama Large Millimeter/submillimeter Array (ALMA) at 226 GHz (with a mass sensitivity of $5\sigma = 0.2 M_{\odot}$ at 10 K). We discovered that at least a binary system is forming inside this region, with an additional nearby bow-like structure ($\lesssim 1000$ au) that could add an additional member to the stellar system. These three sources are located at the center of the gravitational potential well of the ALMA1 region and the larger MM1 cluster. The emission from CH₃OH (and many other tracers) is extended (> 1000 au), revealing a common envelope toward the binary system. We use CH₂CHCN line emission to estimate an inclination angle of the rotation axis of 26° with respect to the line of sight based on geometric assumptions and derive a kinematic mass of the primary source (protostar+disk) of $3.0 M_{\odot}$ within a radius of 230 au. Using SiO emission, we find that the primary source drives the large-scale outflow revealed by previous observations. Precession of the binary system likely produces a change in orientation between the outflow at small scales observed here and large scales observed in previous works. The bow structure may have originated from the entrainment of matter into the envelope due to the widening or precession of the outflow, or, alternatively, an accretion streamer dominated by the gravity of the central sources. An additional third source, forming due to instabilities in the streamer, cannot be ruled out as a temperature gradient is needed to produce the observed absorption spectra.

Unified Astronomy Thesaurus concepts: Star formation (1569); Star forming regions (1565); Massive stars (732)

1. Introduction

High-mass stars are born in clusters or associations of stars. They are thus likely to form binary or multiple stellar systems. During the gravitational collapse of a molecular cloud, the initial physical conditions define how the cloud will fragment. Core fragmentation can create bound systems that can ultimately result in wide binary systems (e.g., Krumholz et al. 2007; with wider fragments forming at distances larger than 1000 au). On the other hand, when the cores have evolved enough that a disk forms, gravitational instabilities allow the development of substructures in the disk, e.g., spiral arms. These can sporadically feed the embedded protostar (e.g., Meyer et al. 2018) or aid the formation of additional companions to the central object if they fragment and grow to become gravitationally unstable (e.g., Mignon-Risse et al. 2021 with fragments forming within 1000 au). Finally, when the stars form a cluster and the system relaxes, close encounters can also allow the formation of binary or multiple systems (e.g., Krumholz et al. 2012).

Given the relatively larger distances of high-mass star-forming regions, resolving core and disk fragmentation requires

high-angular-resolution observations achievable only with the current generation of interferometers, such as the Atacama Large Millimeter/submillimeter Array (ALMA). Observations of resolved single (e.g., G345.4938+01.4677, Guzmán et al. 2020; AFGL 4176, Johnston et al. 2020a; G17.64+0.16, Maud et al. 2019) and binary systems (e.g., IRAS 07299–1651, Zhang et al. 2019; IRAS 16547–4247, Tanaka et al. 2020; and potentially W33A, Maud et al. 2017) hosting high-mass protostars have shown a diversity of environments. The observations of high-mass binary systems show that each component has its individual accretion disk, which is in turn fed by a circumbinary disk. Additional substructures detected toward these sources are large-scale streamers at > 1000 au scales as revealed by the 1.3 mm continuum of IRAS 07299–1651 (Zhang et al. 2019) and of W33A as revealed by 0.8 mm continuum and molecular line emission (Izquierdo et al. 2018a) and outflow cavity walls from the continuum observations of IRAS 16547–4247 (Tanaka et al. 2020).

As part of the Digging into the Interior of Hot Cores with ALMA (DIHCA) survey, we are studying the prevalence of binary systems in a sample of 30 high-mass star-forming regions (P. Sanhueza 2022, in preparation). In our first case study of the survey (Olguin et al. 2021, hereafter Paper I), we analyzed ALMA 1.3 mm observations of the high-mass source G335.579–0.272 MM1 (distance $d = 3.25$ kpc, hereafter G335 MM1). These observations revealed five continuum sources, with two of them associated with radio emission



Original content from this work may be used under the terms of the [Creative Commons Attribution 4.0 licence](https://creativecommons.org/licenses/by/4.0/). Any further distribution of this work must maintain attribution to the author(s) and the title of the work, journal citation and DOI.

Table 1
ALMA 12 m Observations of G335 MM1 for the DIHCA Survey

| Configuration | Date | Antennas | Baseline Range |
|---------------|----------|----------|----------------|
| Compact | 2016 Nov | 41 | 18.6–1100 m |
| Extended | 2019 Jul | 42 | 92.1–8500 m |

observed by Avison et al. (2015): ALMA1 (radio MM1a) and ALMA3 (radio MM1b). The most massive source is ALMA1 with an estimated mass of its gas reservoir of $6.2 M_{\odot}$ (Paper I). Its radio emission has a spectral index whose origin can be attributed to a hypercompact H II region (HC H II; Avison et al. 2015). Previous ALMA observations of ALMA1 show that the matter around the central source is infalling and rotating at large scales and expanding within the central region (Paper I). This source is driving a molecular outflow with an inclination angle, i , between 57° and 76° as derived from the outflow geometry (Avison et al. 2021) and a position angle P. A. $\sim 210^{\circ}$ (Paper I). We note that when G335 MM1 was originally discovered (Peretto et al. 2013), this object was recognized as one of the most massive cores in the Galaxy contained in a 10,000 au diameter (see also Stephens et al. 2015). Therefore, one of the goals of the DIHCA survey is to reveal what is hidden deeply embedded in massive cores and whether they monolithically form high-mass stars or fragment in binary (multiple) systems.

We present here high-resolution ALMA observations that resolve substructures within the high-mass core G335 MM1 ALMA1. Section 2 describes the observations. The results are presented in Section 3. We discuss the origin of the substructures in Section 4. Finally, our conclusions are presented in Section 5.

2. Observations

We observed G335 MM1 with ALMA at 226.2 GHz (1.33 mm) during 2019 July (Project ID: 2016.1.01036.S; PI: Sanhueza). The 42 antennas of the 12 m array covered a baseline range of 92.1 to 8500 m in a configuration similar to C43-8 (hereafter extended configuration). As a result, the resolution of the observations was $\sim 0''.05$ (~ 160 au) with a maximum recoverable scale (MRS) of $0''.78^9$ and primary beam FWHM of $25''.1$. The observations were performed in single-pointing mode. Table 1 summarizes the observations of G335 MM1 undertaken for the DIHCA survey. The four spectral windows and resolution of the observations are equivalent to those presented in Paper I. To summarize, the spectral windows cover the 216.9–235.5 GHz range with a spectral resolution of 976.6 kHz (~ 1.3 km s $^{-1}$).

The data were reduced using CASA (v5.4.0–70; McMullin et al. 2007), with J1617–5848, J1427–4206, and J1650–5044 as flux, bandpass, and phase calibrators, respectively. We then self-calibrated the data and produce continuum maps from line-free channels following the steps detailed in Paper I. In addition

⁹ Calculated using Equation (7).7 from the ALMA Technical Handbook (<https://almascience.nao.ac.jp/documents-and-tools/cycle8/alma-technical-handbook>):

$$\theta_{\text{MRS}} \approx \frac{0.983\lambda}{L_5}, \quad (1)$$

with $\lambda = 1.33$ mm and L_5 the fifth percentile baseline length.

to these extended configuration observations, we combined the continuum-subtracted visibilities with those from Paper I (hereafter compact configuration; see Table 1) to recover large-scale diffuse emission. We produced continuum maps for the extended and combined data sets. These maps were produced using the TCLEAN task in CASA with Briggs weighting and a robust parameter of 0.5. The map of the combined data set is shown in Figure 1(a), and a zoom-in view of the central region from the extended configuration image is shown in Figure 1(b) for a better contrast of the sources. The noise level achieved by the continuum extended configuration observations alone is $57 \mu\text{Jy beam}^{-1}$, while for the combined data set, the noise level is $66 \mu\text{Jy beam}^{-1}$. The beam FWHM of the continuum CLEAN maps is $0''.061 \times 0''.040$ P.A. = 48° and $0''.064 \times 0''.043$ P.A. = 48° for the extended and combined continuum images, respectively. The MRS of the combined data set is $1''.74$.

Data cubes for lines of interest were produced using the automatic masking procedure YCLEAN (Contreras et al. 2018). Similar to the continuum, we produced data cubes for the extended and combined data sets. A noise level of roughly 2 mJy beam^{-1} per channel (~ 17 K), with a channel width of ~ 0.6 km s $^{-1}$, was achieved in both data sets and across all spectral windows.

Flux measurements in this work are measured in the primary-beam-corrected images, while figures present uncorrected data.

3. Results

3.1. Core Fragmentation

The single source ALMA1 resolved by previous $0''.3$ resolution ALMA observations is further divided into at least four continuum sources identified in the combined map. Figure 1(a) shows the continuum observations with the new sources labeled. Table 2 lists the properties of the sources measured from a 2D Gaussian fit to the continuum emission. We use the combined data set to measure the source fluxes. The brightest source (ALMA1a) has a close companion (ALMA1b) separated by ~ 85 mas, corresponding to a projected distance of ~ 280 au. The two additional sources (ALMA1c and ALMA1d) are located at a projected distance of 2500 and 1300 au from ALMA1a, respectively.

An additional structure is observed to the south of ALMA1a at a projected distance of ~ 780 au ($0''.24$ measured peak to peak). This bow-shaped object is connected to the central region by an arc-shaped structure. This source is labeled “bow” in Figure 1, and its properties are listed in Table 2. We avoid categorizing this structure as a core because of its shape and location, which is close to the large-scale molecular outflow (P.A. = 210° ; Paper I). We discuss different scenarios for the origin of this source in Section 4. In order to facilitate the analysis, we will refer to the region enclosing the sources ALMA1a and ALMA1b, and the bow as the central region, as shown in Figure 1(b). This region encompasses $\sim 70\%$ of the flux density of ALMA1 ($F_{\text{ALMA1}} = 0.74$ Jy). The remaining $\sim 30\%$ is produced by ALMA1c and extended/fainter structures, e.g., the arc-shaped structure in Figure 1(a).

3.2. Line Emission

Table 3 summarizes the molecules and transitions analyzed here and the type of line profile observed toward the brightest

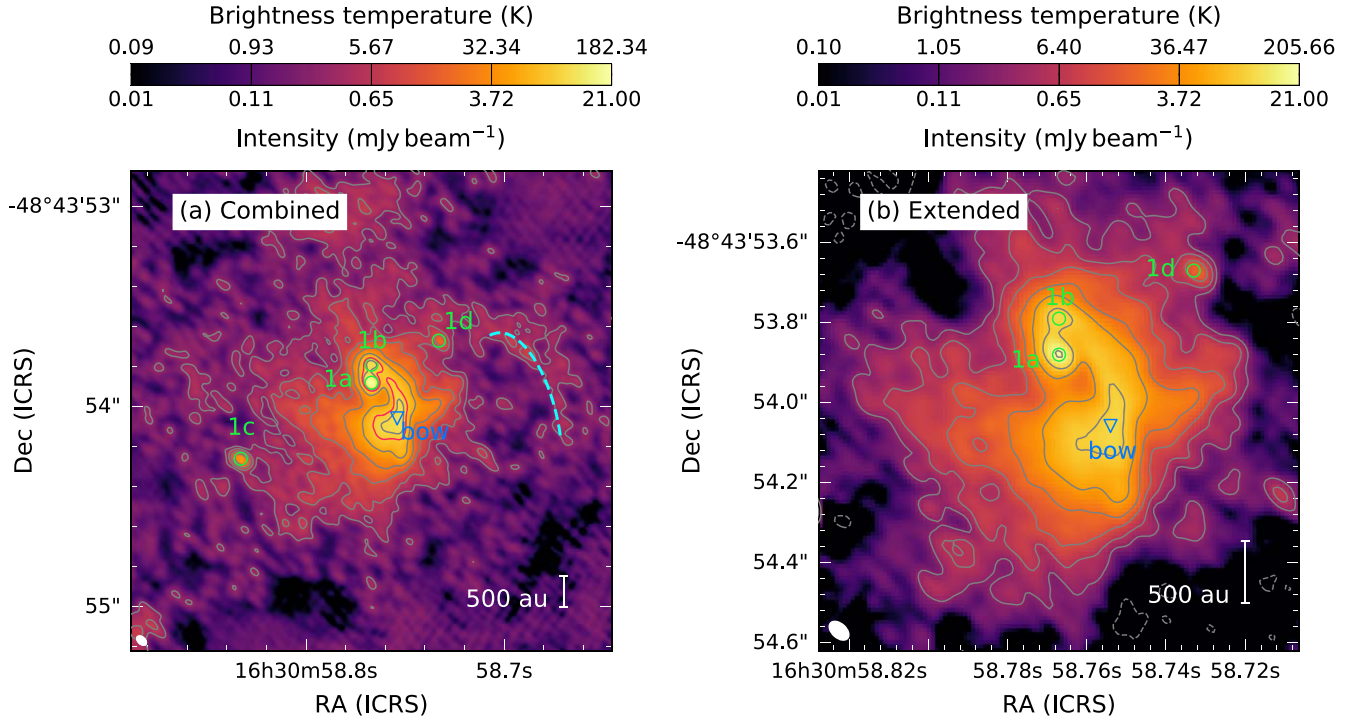


Figure 1. ALMA continuum maps of G335 ALMA1 at 1.3 mm in color scale and contours from (a) the combined data set and (b) the extended data set. (a) The gray contours levels are $-3, 5, 10, 20, 40, 80, 160 \times \sigma_{\text{cont}}$, with $\sigma_{\text{cont}} = 66 \mu\text{Jy beam}^{-1}$. The dashed light blue line shows the arc-shaped structure described in Paper I. The $130 \times \sigma_{\text{cont}}$ level is shown in red contours. (b) The gray contours levels are $-6, -3, 5, 10, 20, 40, 80, 160, 320 \times \sigma_{\text{cont}}$, with $\sigma_{\text{cont}} = 57 \mu\text{Jy beam}^{-1}$. The green circles and labels mark the peak position of the sources identified within this region and are labeled in order of brightness. The position of the bow structure peak is marked with a blue triangle. The beam size is shown in the lower-left corner and corresponds to a scale of ~ 160 au for both data sets.

Table 2
Continuum Source Properties

| ALMA Source | R.A. (ICRS) [h:m:s] | Decl. (ICRS) [°: ': "] | I_{peak} (mJy beam $^{-1}$) | T_b (K) | F_{total} (mJy) | FWHM (mas) | v_{LSR} (km s $^{-1}$) |
|------------------|------------------------|---------------------------|--|--------------|-----------------------------|------------------|-------------------------------------|
| 1a | 16:30:58.767 | -48:43:53.87 | 20.6 | 179 | 69 ± 6 | 101×80 | -46.9 |
| 1b | 16:30:58.767 | -48:43:53.80 | 11.8 | 103 | 72 ± 3 | 120×115 | -46.9 |
| 1c | 16:30:58.833 | -48:43:54.26 | 4.7 | 41 | 7.2 ± 0.4 | 47×35 | -46.9 |
| 1d | 16:30:58.733 | -48:43:53.67 | 2.1 | 18 | 6.8 ± 1.1 | 103×90 | $[-56.5, -53.2]$ |
| bow ^a | ... | ... | 12.1 | 105 | 93 | ... | ... |

Notes. Fluxes measured on the combined primary-beam-corrected data set. The FWHM is deconvolved from the beam.

^a Fluxes measured within the 130σ contour with $\sigma = 66 \mu\text{Jy beam}^{-1}$. This is an arbitrary number defined to trace most of the bow emission without including ALMA1a and ALMA1b.

Table 3
Molecular Lines and Transitions Analyzed

| Molecule | Transition | Freq. (GHz) | E_u (K) | Line Profile | Reference |
|--------------------------|---|----------------|--------------|-----------------|-----------|
| SiO | $J = 5-4$ | 217.1049800 | 31 | self-absorbed | (2) |
| SO | $^3\Sigma v = 0 J_K = 6_5-5_4$ | 219.949442 | 35 | self-absorbed | (1) |
| ^{13}CO | $J = 2-1$ | 220.4758072 | 16 | inverse P Cygni | (2) |
| CH_3CN | $J_K = 12_3-11_3$ | 220.7090165 | 133 | inverse P Cygni | (1) |
| CH_2CHCN | $v_{11} = 1 J_{K_a, K_c} = 23_{15,8} - 22_{15,7}$ | 219.5207483 | 929 | single | (1) |
| CH_3OH | $E_1 v_t = 0 J_K = 25_3-24_4$ | 219.983675 | 802 | single | (2) |
| | $E_1 v_t = 0 J_K = 23_5-22_6$ | 219.993658 | 776 | single | (2) |

References. (1) Jet Propulsion Laboratory (JPL, Pickett et al. 1998); (2) Cologne Database for Molecular Spectroscopy (CDMS, Müller et al. 2005).

continuum source. As in the compact configuration observations, several molecular-line transitions are observed in general. However, toward sources ALMA1a and ALMA1b, we observe self-absorbed transitions of, e.g., H_2CO , and inverse P Cygni

profiles of, e.g., CH_3CN (see Section 3.4). Figure 2 shows example spectra toward different positions in one of the spectral windows. The bow is devoid of molecular lines for the most part, and molecules tracing cold, lower density gas, like

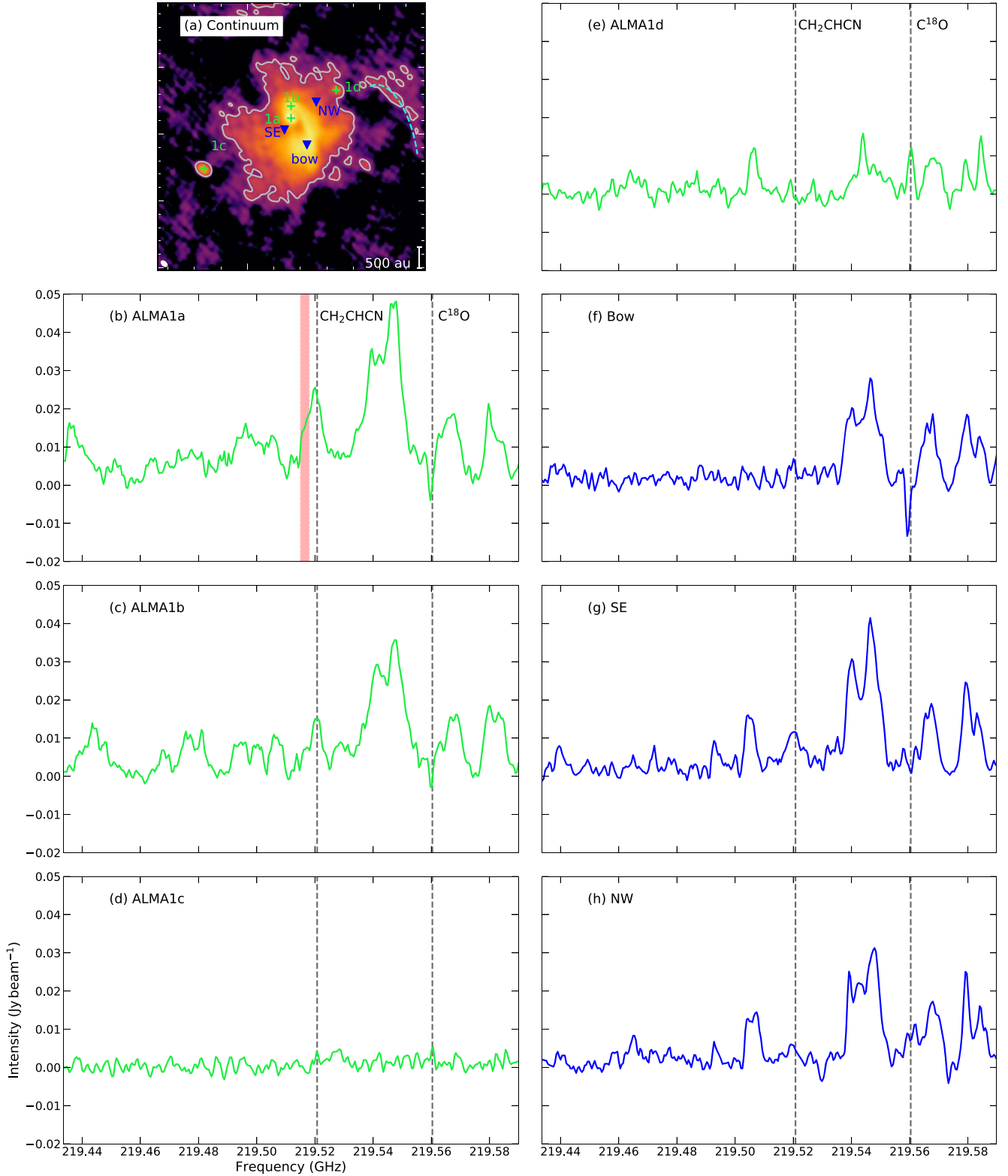


Figure 2. Example spectra toward selected positions marked in the dust continuum image displayed in panel (a). The red shaded area highlights the high-velocity red wing of the CH_2CHCN line (see Section 3.4).

CO isotopologues, are observed in absorption as shown in Figure 2(f) for C^{18}O . It is worth noticing that many lines start to disappear toward the continuum peaks when compared to the compact configuration data from Paper I.

We detect faint emission that may be associated with blueshifted $\text{H}30\alpha$ emission ($\nu = 231.90092784$ GHz). Alternative lines in the

same frequency range (231.8986396–231.9035225 GHz) include transitions of $^{33}\text{SO}_2$ with the one with the highest Einstein coefficient at 231.9002488 GHz (CDMS; $|\Delta\nu_{\text{H}30\alpha}| = 0.7$ MHz), $\text{CH}_3\text{C}^{15}\text{CN}$ at 231.90223 GHz (JPL; $|\Delta\nu_{\text{H}30\alpha}| = 1.3$ MHz), and other carbon-bearing molecules. Figure 11 in Appendix A shows the zeroth- and first-order moment maps. The emission is

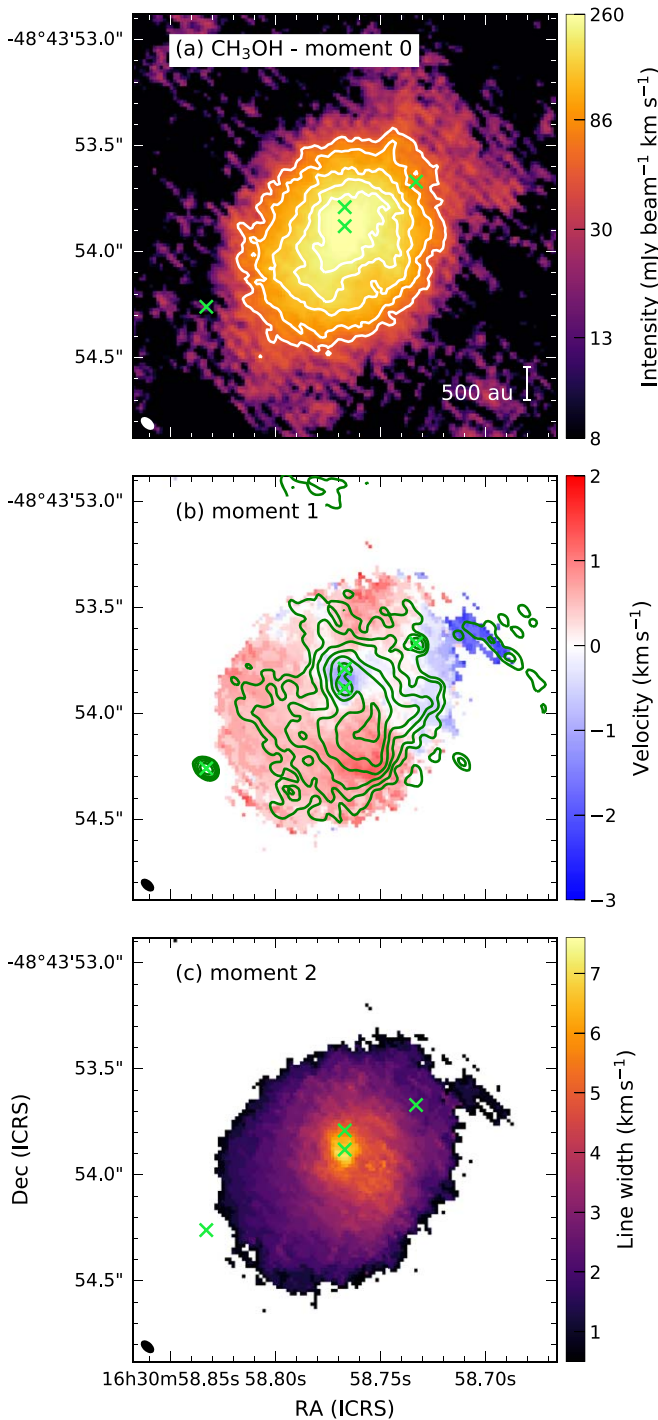


Figure 3. $\text{CH}_3\text{OH } J_K = 23_5-22_6$ moment maps from the combined data set. (a) Zeroth-order moment map. Contour levels correspond to 5, 8, 12, 16, $20 \times \sigma_{\text{rms}}$, with $\sigma_{\text{rms}} = 11 \text{ mJy beam}^{-1} \text{ km s}^{-1}$. (b) First-moment map with continuum emission in contours from Figure 1(b). Zero systemic velocity corresponds to the source $v_{\text{LSR}} (-46.9 \text{ km s}^{-1})$. (c) Second-order moment map. The location of the continuum sources is marked with green crosses. The beam size is shown in the lower-left corner.

distributed in the direction of the blueshifted outflow lobe surrounding the sources ALMA1a and ALMA1b and the bow. The emission toward these sources is attenuated or extincted by the optically thicker continuum (see below). The diameter of the emission is roughly 2600 au (0.01 pc), which is larger than the size of the H II region estimated by Avison et al. (2015, $\sim 95 \text{ au}$). Given its distribution, velocity shift, and extent, the H30 α emission may

be associated with gas ionized by photons escaping through the less dense medium of the outflow cavity.

3.3. Physical Properties

Figure 3 shows the moment maps of the $\text{CH}_3\text{OH } J_K = 23_5-22_6$ transition listed in Table 3 as an example. The moments are calculated in a spectral window with a width of 20 channels ($\sim 12 \text{ km s}^{-1}$) centered at the line frequency, and the first and second moments are calculated from emission over 5σ with $\sigma = 2 \text{ mJy beam}^{-1}$. Figure 3(a) shows that the emission is extended, tracing gas around the central region of ALMA1 (including 1a, 1b, and the bow), in what seems to be a common reservoir of gas. As such, we use the CH_3OH transitions listed in Table 3 to derive physical properties, namely the circumstellar gas temperature, CH_3OH column density, velocity distribution, and line width. We fitted the spectra on a pixel-by-pixel basis using the CASSIS software¹⁰ (Vastel et al. 2015) and the CDMS molecular database (Müller et al. 2005). The fitting assumes local thermodynamic equilibrium (LTE) in a column of gas with constant density and a Gaussian line shape. An additional parameter is required for the fit, the source size, to determine the beam dilution factor. We set the source size to $1''$, which is roughly the size of the CH_3OH emission because the source is well resolved. We limit the fit only to data over the 5σ level in the zeroth-order moment map (see Figure 3(a)). We use the Markov Chain Monte Carlo tasks built in CASSIS to explore the parameter space. In general, the lines are well fitted with a single temperature/density component, resulting in reduced χ^2 values below 2.

Figure 4 shows the distribution of the fitted physical properties, while the error maps for these properties and the reduced- χ^2 map from the fit are presented in Appendix A, Figure 12. The fitted spectra toward the continuum peak positions of ALMA1a, ALMA1b, and the bow are presented in Appendix A, Figure 13. The column density peaks are located at the position of sources ALMA1a and ALMA1b and toward the bow structure, with average values over a beam-sized region between $2-9 \times 10^{19} \text{ cm}^{-2}$. Note that the errors in column density are particularly large in the region surrounding the sources; this is likely due to the number of lines fitted and a lower signal-to-noise ratio (S/N). Similarly, the average temperatures around these sources are $\sim 220 \text{ K}$. Table 4 lists the column density and temperature values for each source and the median values of the whole ALMA1 region. We note, however, that higher temperatures are achieved around the sources. The velocity distribution and line-width maps in Figures 4(c) and (d) are consistent with the first- and second-moment maps in Figures 3(b) and (c), respectively.

Following Paper I and assuming optically thin dust emission, we calculate the gas mass as

$$M_d = \frac{F_\nu d^2 R_{gd}}{\kappa_\nu B_\nu(T_d)}, \quad (2)$$

with $F_{1.3\text{mm}}$ the flux density from Table 2, $d = 3.25 \text{ kpc}$ the source distance, $R_{gd} = 100$ the gas-to-dust mass ratio, $\kappa_{1.3\text{mm}} = 1 \text{ cm}^2 \text{ gr}^{-1}$ the dust opacity (Ossenkopf & Henning 1994), and B_ν the Planck blackbody function. We also calculate

¹⁰ CASSIS has been developed by IRAP-UPS/CNRS (<http://cassis.irap.omp.eu>).

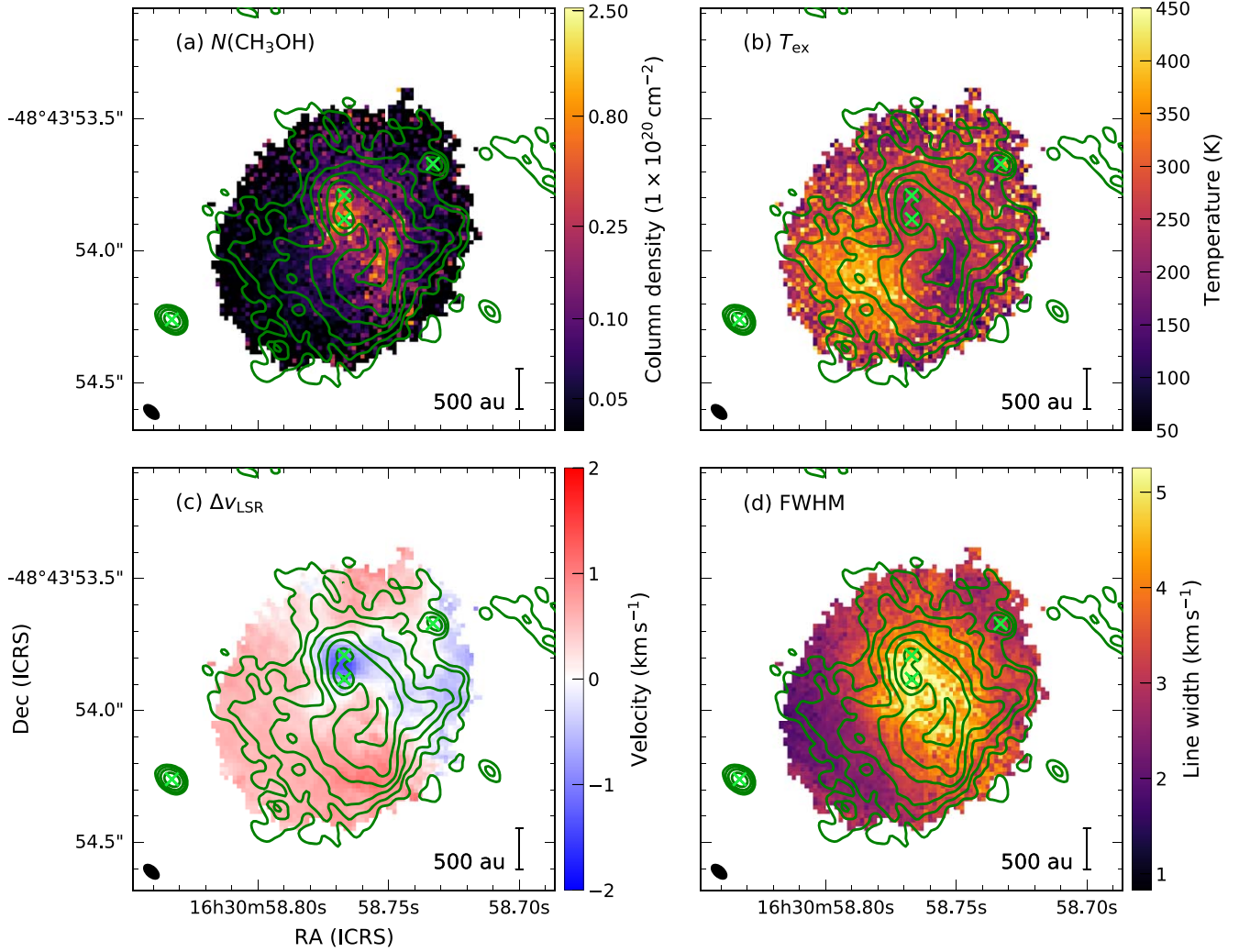


Figure 4. CH₃OH LTE modeling results. (a) CH₃OH column density. (b) Excitation temperature map. (c) Velocity shift with respect to the systemic velocity. Zero systemic velocity corresponds to the source v_{LSR} (-46.9 km s^{-1}). (d) Line FWHM map. Contour levels correspond to $5, 8, 12, 16, 20 \times \sigma_{\text{rms}}$, with $\sigma_{\text{rms}} = 11 \text{ mJy beam}^{-1}$. The green contours correspond to the continuum emission from the extended configuration, Figure 1(b). The location of the continuum sources are marked with green crosses. The beam size is shown in the lower-left corner.

the peak H₂ column density, defined as

$$N_{\text{H}_2}^{\text{peak}} = \frac{I_{\nu} R_{\text{gd}}}{B_{\nu}(T_d) \kappa_{\nu} / \mu_{\text{H}_2} m_{\text{H}}}, \quad (3)$$

with $I_{1.3\text{mm}}$ the peak intensity from Table 2, $\mu_{\text{H}_2} = 2.8$ the molecular weight per hydrogen molecule (e.g., Kauffmann et al. 2008), and m_{H} the atomic hydrogen mass. The lack of line emission makes an accurate estimation of the dust temperature for all sources difficult, hence we have adopted different approaches to estimate the dust temperature. For sources ALMA1a and ALMA1b we use the temperature estimates from the fit to the CH₃OH emission. Sources ALMA1c and ALMA1d likely host low-mass protostars, thus we use a dust temperature of 20 K. The mass and column density of the sources are listed in Table 4 (optically thin heading).

Note that the optical depth $\tau_{\nu} = \mu_{\text{H}_2} m_{\text{H}} \kappa_{\nu} R_{\text{gd}}^{-1} N_{\text{H}_2}^{\text{peak}} = 1$ when $N_{\text{H}_2}^{\text{peak}} = 2.1 \times 10^{25} \text{ cm}^{-2}$. Thus, for sources ALMA1a and ALMA1b and the bow structure, the dust emission is becoming optically thick. This is also true for the column density derived from CH₃OH for abundances as high as 10^{-6}

(e.g., Menten et al. 1986; Crockett et al. 2014). We thus consider the values of the column densities for sources ALMA1a and ALMA1b and the bow as lower limits. For sources ALMA1c and ALMA1d, the temperatures may be higher, in which case the column densities are an upper limit.

Similarly, the masses of ALMA1a, ALMA1b, and the bow structure are also lower limits. These sources are located at the center of the gravitational potential well of ALMA1 ($6\text{--}19 M_{\odot}$; see Paper I and Table 4) as shown in Appendix A, Figure 14 and the larger MM1 clump ($790 M_{\odot}$; Avison et al. 2015, see also their Figure 3). Hence, the gas reservoir around the continuum sources can be replenished and the forming stars can continue growing by following scenarios such as competitive accretion (e.g., Smith et al. 2009) or global hierarchical collapse (Vázquez-Semadeni et al. 2019); see also discussions in Contreras et al. (2018) and Sanhueza et al. (2017, 2019). The masses are derived under the optically thin approximation although lower limits are similar to those found in other high-mass binary systems at equivalent radii (e.g., 0.2 and $0.04 M_{\odot}$ at 150 au for the detected objects in IRAS 16547–4247; Tanaka et al. 2020). Contribution from free-free emission also becomes important for the mass and column

Table 4
Source Physical Properties

| ALMA Source | R^a (au) | T (K) | L (L_\odot) | M_d (M_\odot) | $N_{\text{H}_2}^{\text{peak}}$ (10^{25} cm^{-2}) | $N_{\text{CH}_3\text{OH}}$ (10^{19} cm^{-2}) |
|-----------------|---------------|-------------|----------------------|------------------------|---|---|
| Optically thin | | | | | | |
| 1 ^b | 710 | 265 | ... | 7.0 | 0.4 | 0.5 |
| 1a | 149 | 230 ± 9 | ... | >1.0 | >1.7 | 8.4 ± 3.6 |
| 1b | 192 | 220 ± 5 | ... | >1.1 | >1.0 | 5.7 ± 2.0 |
| 1 c | 66 | 20 | ... | 1.5 | 5.8 | ... |
| 1d | 157 | 20 | ... | 1.5 | 2.6 | ... |
| bow | 300 | 220 ± 2 | ... | >1.4 | >1.0 | 2.5 ± 0.2 |
| Optically thick | | | | | | |
| 1a | 149 | 179 | >950 | ... | ... | ... |
| 1b | 192 | 103 | >170 | ... | ... | ... |
| bow | 300 | 105 | >480 | ... | ... | ... |

Notes. The temperature and CH_3OH column density of ALMA1a and ALMA1b are averages over a beam-sized area with a radius of 26 mas from the maps in Figure 4, while their errors are calculated using $\sigma = N^{-1} \sqrt{\sum \sigma_i^2}$, with the N corresponding values of σ_i in Appendix A, Figure 12. The same properties for the bow structure are measured over the same region as the measured fluxes in Table 2 (130σ level).

^a The radius of ALMA1 is from Paper I, while radius of sources 1a–1d corresponds to half of the geometric mean of the deconvolved sizes (FWHM) from Table 2. The radius of the bow is determined by the area of the 130σ level with $A_{130\sigma} = \pi r^2$. This is an arbitrary value as the source is non-Gaussian.

^b The temperature and CH_3OH column density correspond to the median values over the ALMA1 region from the maps in Figure 4. The mass and peak column density values are calculated from data in Paper I: $F_{\text{total}} = 566 \text{ mJy}$ and $I_{\text{peak}} = 209.8 \text{ mJy beam}^{-1}$.

density calculations at the scales of the observations presented here. Following the fitting of the free–free and dust continuum emission of Avison et al. (2015) with a turnover frequency of $\sim 22 \text{ GHz}$, a contribution from free–free emission of less than 5 mJy was estimated in Paper I, which is roughly an order of magnitude lower than the flux density of the brightest source. However, HC H II regions may have higher turnover frequencies if a density gradient is present (Lizano 2008 and references therein). Figure 5 shows the spectral energy distribution with a power-law fit to the radio data. Assuming the radio emission is only due to free–free emission, we expect its contribution at 220 GHz to be 42 mJy , which is roughly 60% of the continuum emission of ALMA1a at the same frequency and hence nonnegligible. Nevertheless, the tentative $\text{H}30\alpha$ emission in Figure 11 in Appendix A indicates that the free–free contribution may be more extended, hence contributing less to the continuum of each individual millimeter source.

In the optically thick limit, the thermal radiation can be approximated by blackbody radiation, and the dust brightness temperature, T_b , converges to the dust temperature. Table 2 lists the values of the brightness temperature. Only the values of the brightness temperature and the temperature from CH_3OH for ALMA1a are relatively similar. We estimate the luminosity of the sources by using

$$L = 4\pi r^2 \sigma_{\text{sb}} T^4, \quad (4)$$

with r the source radius and σ_{sb} the Stefan–Boltzmann constant. The values of the luminosity for $T = T_b$ are listed in Table 4 (optically thick heading). These values are likely lower limits as the beam-filling factor may be different lower than unity, due to clumpiness within the source. Based on the disk

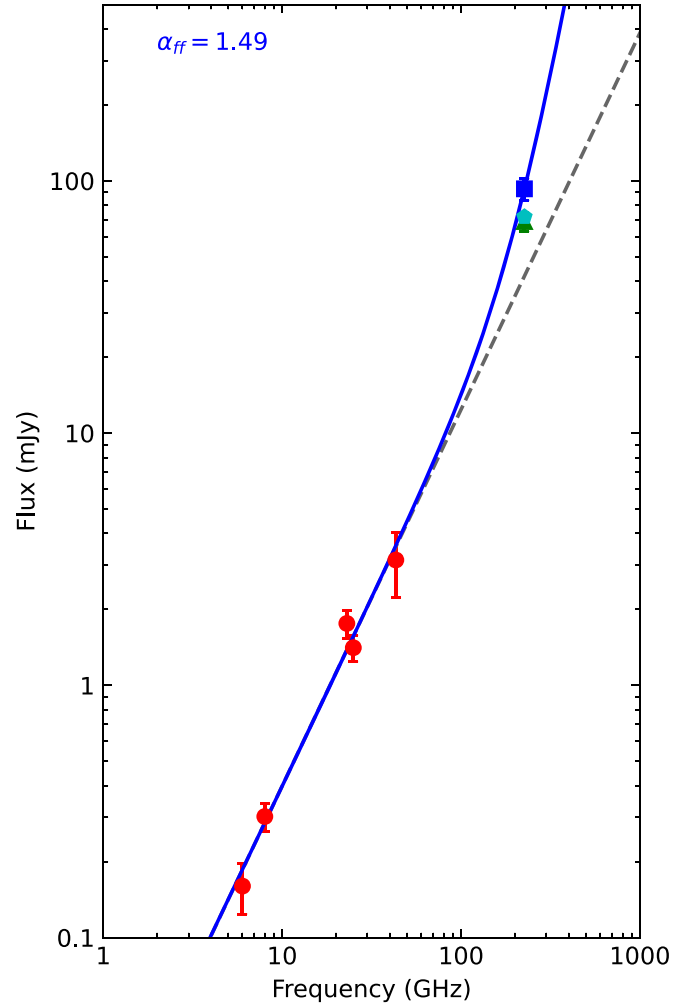


Figure 5. Radio and millimeter SED of G335 ALMA1. The blue square is the contribution from the bow structure (see Table 2). Red dots correspond to the radio measurements of G335 MM1a from Avison et al. (2015). The green triangle and cyan pentagon correspond to the contributions from ALMA1a and 1b, respectively. The blue line corresponds to a model with two power-law distributions accounting for the contributions of dust and free–free emission and assuming that the radio free–free emission is produced by the bow structure. The dashed line corresponds to a power law fitted to the radio data.

accretion models of Hosokawa et al. (2010), at the estimated luminosity, the high-mass (proto)stars would have accumulated masses in excess of $4\text{--}5 M_\odot$ and would be on or have finished the bloated stage where the luminosity sharply increases depending on the accretion rate.

3.4. Kinematics

The large-scale emission from CH_3OH is likely produced by a combination of motions. Toward the blueshifted outflow lobe (southwest), we see blueshifted emission and wider line widths as shown by both the observations and model (Figures 3 and 4). This pattern was also observed in the high-mass YSO AFGL-2591 and interpreted as gas in the surface of the envelope cavity walls being shocked by the outflow (Olguin et al. 2020). Elsewhere, the velocity pattern shows a central blueshifted region surrounded by redshifted emission. Upon inspection of the spectra between the sources ALMA1a and 1b, we note that the spectra have blue wings that produce the blue spot at the center rather than blue skewed profiles indicative of

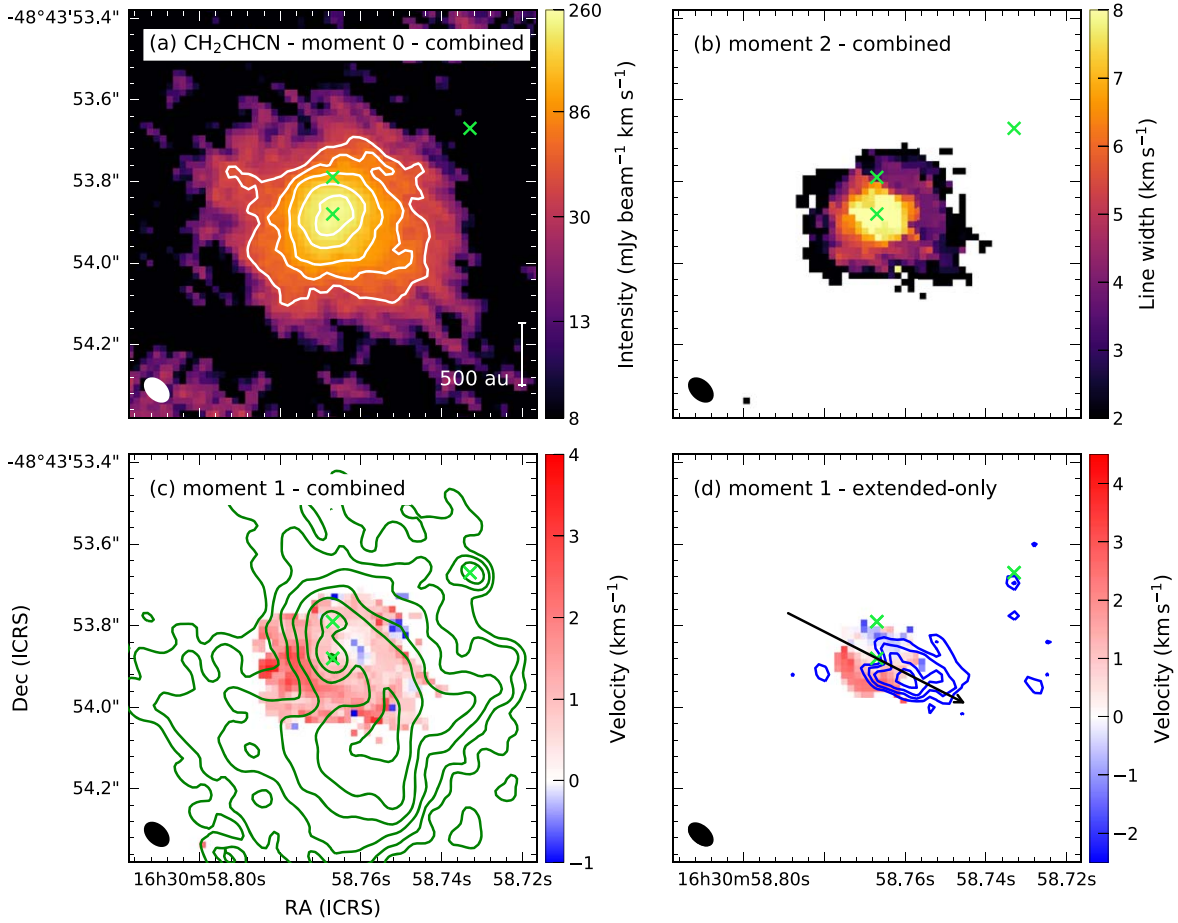


Figure 6. CH₂CHCN moment maps. (a) Zeroth-moment map. Contour levels are 5, 8, 12, 18, 24 $\times \sigma_{\text{rms}}$, with $\sigma_{\text{rms}} = 8.6 \text{ mJy beam}^{-1} \text{ km s}^{-1}$. (b) Second-moment map of the emission over the 5σ level with $\sigma = 2 \text{ mJy beam}^{-1}$ the noise level per channel. (c) First-moment map of the emission over 5σ level from the combined data set. The green contours correspond to the continuum emission from Figure 1(b). Zero systemic velocity corresponds to the source v_{LSR} (-46.9 km s^{-1}). (d) First-moment map from the extended configuration data set. The arrow indicates the direction perpendicular to the velocity gradient (P.A. = 150°), i.e., along the rotation axis. Blue contours correspond to the blueshifted outflow lobe emission from SiO (see Figure 7). The locations of the continuum sources are marked with green crosses. The beam size is shown in the lower-left corner.

infall (e.g., Estalella et al. 2019, Paper I). These can be produced by the motions of two or more gas components, e.g., the combined effect of the rotation of the cores, as well as the blueshifted lobe of the outflow closer to the source.

Among the myriad of lines in the spectrum, we could find only one single-peaked line tracing the region close to the continuum sources. The line emission is likely produced by a transition of CH₂CHCN (vinyl cyanide) and traces the inner region of ALMA1a. We note that vinyl cyanide has been previously detected in extreme high-mass star formation environments, such as Orion KL (López et al. 2014) and Sgr B2(N) (Belloche et al. 2013). Figure 6 shows the moment maps from CH₂CHCN. The zeroth-order moment map in Figure 6(a) peaks at the same position of ALMA1a and shows that the line is tracing the inner 500 au of the source. The velocity distribution in the first-moment map from the emission traced by the combined observations (Figure 6(c)) is mostly shifted toward the red. This is probably produced by high-velocity red wings (see the red shaded area in Figure 2(b)) similar to those observed in HDCO in Paper I. On the other hand, the first-moment map from the extended configuration data (Figure 6(d)) shows a velocity gradient in the northwest to southeast direction, perpendicular to the molecular outflow. We

measure a velocity gradient with P.A. = $150^\circ \pm 28^\circ$ in a region about the size of the beam at the continuum position.

From the velocity gradient we also estimate the mass of the ALMA1a source inside a radius r . We measure a velocity difference between the blue- and redshifted lobes of the first-moment map in Figure 6(d) of 3 km s^{-1} at points separated by $0''.14$ (455 au) in a slit passing through the source position and with a P.A. equal to that of the velocity gradient. The velocity along the line of sight is thus $|v_{\phi, \text{obs}}| = 1.5 \text{ km s}^{-1}$ at a distance of $r = 228 \text{ au}$ from the source. For a purely rotating disk, the velocity of rotation is related to the observed velocity as $|v_{\phi, \text{obs}}| = |v_{\phi}| \sin i$. Assuming Keplerian rotation (see the position-velocity, PV, map in Appendix A, Figure 15) the mass inside r is given by

$$M = \frac{rv_{\phi, \text{obs}}^2}{G \sin^2 i}, \quad (5)$$

with G the gravitational constant. The deconvolved FWHM of the CH₂CHCN emission from a 2D Gaussian fit to the zeroth-order moment maps is $0''.281 \times 0''.252$ and $0''.162 \times 0''.145$ for the combined and extended configuration data, respectively. The inclination angle can be estimated by assuming that the emission comes from a disk with $\cos i = b/a$, where a and b

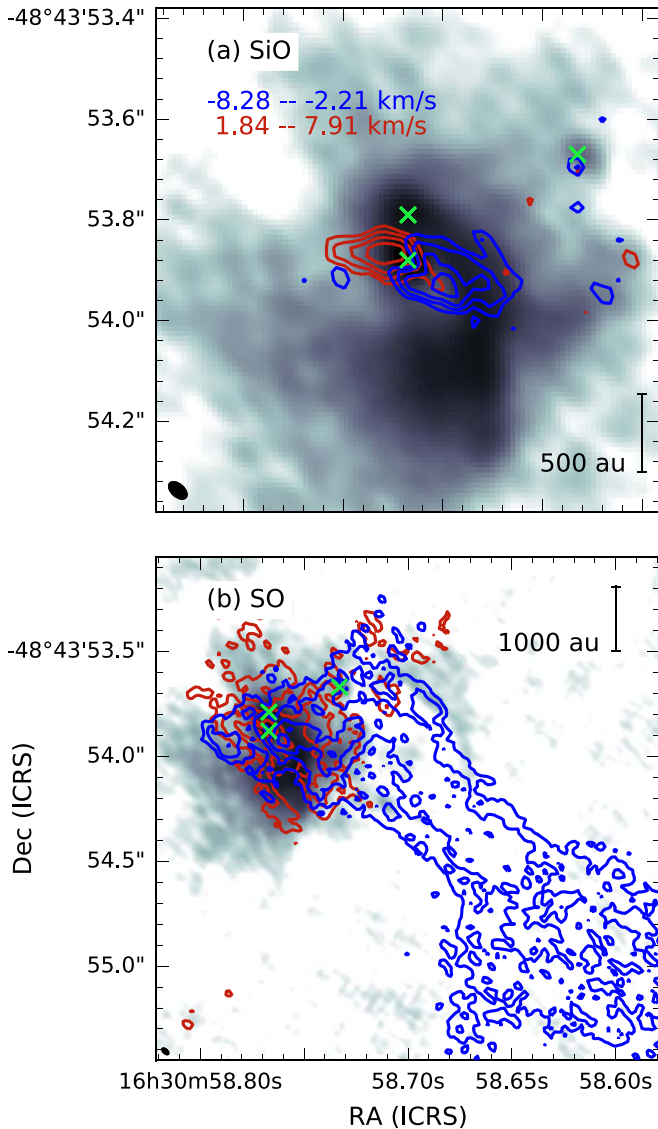


Figure 7. Outflow emission from G335 ALMA1 in contours over the dust continuum. (a) SiO $J=5-4$ red- and blueshifted outflow lobes. Contour levels are 5, 6, 7.2, $8.6 \times \sigma_{\text{rms}}$, with $\sigma_{\text{rms}} = 6 \text{ mJy beam}^{-1} \text{ km s}^{-1}$. (b) SO $J_K=6_5-5_4$ red- and blueshifted emission. Contour levels are 5, 7, 10, 14, $19 \times \sigma_{\text{rms}}$, with $\sigma_{\text{rms}} = 7.2 \text{ mJy beam}^{-1} \text{ km s}^{-1}$. The velocity integration range for each lobe is shown in (a). The locations of the continuum sources are marked with green crosses. The beam size is shown in the lower-left corner.

are the semimajor and -minor axes. We obtain a mean inclination angle of 26° , which is lower than those estimated by Avison et al. (2021, $i=57^\circ$ and 76°). This change in inclination can be the result of precession caused by the binary system. Moreover, the change in orientation of the SiO outflow emission between the small and large scales (see below) indicates that we may be looking into the outflow cavity (lower inclination angle). We thus obtain a star+disk mass of $3 M_\odot$. For a B1-1.5 zero-age main-sequence star (Avison et al. 2015) with a mass of $\sim 7 M_\odot$, the inclination angle would need to be $i \sim 15^\circ$ to explain the observed velocity distribution.

3.4.1. Outflows

We use the SiO $J=5-4$ transition to study the outflow emission. Figure 7 shows the maps from the red- and

blueshifted emission. The zeroth-order moment maps were calculated on the blue- and redshifted sides of the channel closest to the line frequency. We avoided the central five channels (two channels at each side of the central one, equivalent to $\sim 1.2 \text{ km s}^{-1}$) and calculated the moments on a window of 10 channels ($\sim 6 \text{ km s}^{-1}$). The origin of the outflow lobes is located around the source ALMA1a. The direction of the blueshifted emission is slightly inclined to the west (higher P.A.) in comparison to the large-scale outflow shown in Figure 7(b) from SO $J_K=6_5-5_4$ emission. As expected for a disk-outflow system, the P.A. of the SiO blueshifted lobe is close to perpendicular to the CH₂CHCN (disk) velocity gradient and thus coincides with the rotation axis of the disk (P.A. = 240° ; see Figure 6(d), while the large-scale outflow P.A. is closer to 210° . The emission producing the redshifted lobe seems to come from gas escaping through a less dense region of the envelope as shown by the dip in dust continuum emission.

In order to study the interaction of the outflow with the circumstellar gas, we additionally calculated zeroth-moment maps of groups of channels on each side of the line, i.e., similar to channel maps of averaged channels. Each map consists of the zeroth-moment maps of five channels ($\sim 3.3 \text{ km s}^{-1}$). Figure 8 shows the maps on each side of the line and the details of the velocity range of each map. High-velocity blueshifted emission seems to trace the interaction of the outflow/jet with the envelope cavity. In Figures 8(a) and (b), the emission is surrounded by the bow structure and is consistent with the location of wide CH₃OH lines toward the southwest. Figure 8(b) in addition shows SiO emission at the location of a dust lane structure (dashed cyan line). Similarly, the high-velocity redshifted emission is coming from regions closer to the source.

Figure 8 also shows evidence of an additional outflow associated with ALMA1d, with the blueshifted outflow pointing in the northwest direction. Given that both the blue- and redshifted outflow emission appear in Figure 8(b), the systemic velocity of ALMA1d seems to be lower than that of ALMA1a. Note that the C¹⁸O emission in Figure 2(e) is single peaked at roughly the same velocity of the ALMA1 region. However, C¹⁸O is likely tracing gas that belongs to the colder larger cloud rather than to ALMA1d in particular. We thus report a velocity range in Table 2 for source ALMA1d based on the range of Figure 8(b). This difference between the systemic velocities indicates that the system ALMA1a/b and ALMA1d likely belong to the same parsec-scale association but the ALMA1d system is far enough such that there is no sign of interaction between their outflows.

3.4.2. Infall Signatures

In addition to the blue central spot observed in CH₃OH, we observe that several lines that appear in emission in the compact configuration data become optically thick, resulting in inverse P Cygni profiles. In particular, the K ladder of CH₃CN $J=12-11$ toward ALMA1a appears in absorption in the extended configuration data, while in the combined data the transitions with $K > 2$ appear in absorption. Figure 9 shows the $K=3$ transition toward ALMA1a and the PV map from a slit of width $0''.05$ (P.A. = 150°), indicating the “C” shape characteristic of infall (Zhang & Ho 1997). The velocity shift of the line dip is slightly higher (0.4 km s^{-1}) than that of ¹³CO $J=2-1$. We fit a Gaussian function to the line absorption and estimate

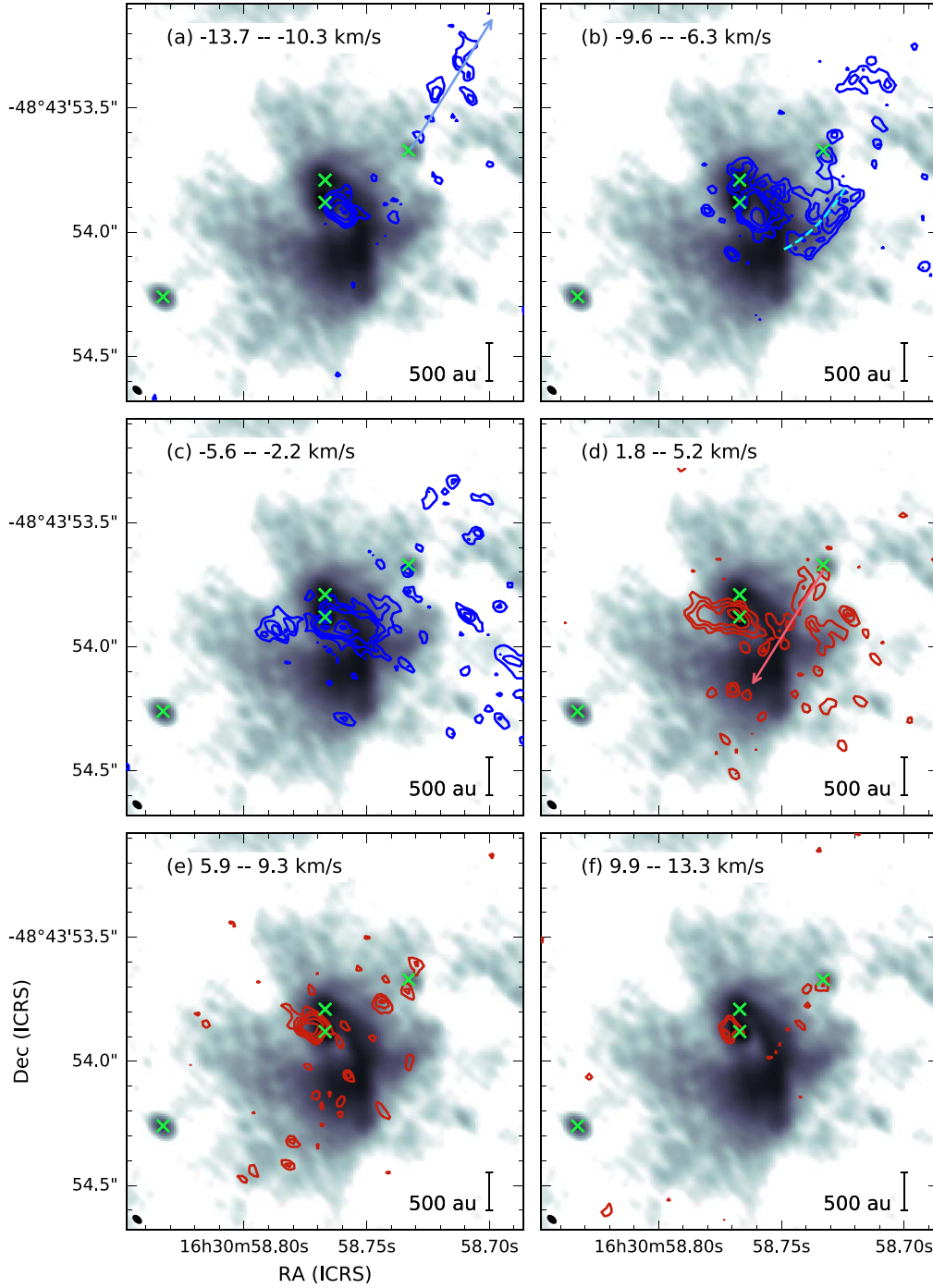


Figure 8. Integrated intensities of SiO over different velocity ranges on each side of the line center (contours) over the dust continuum (gray scale). (a)–(c) correspond to the blueshifted emission and (d)–(f) to the redshifted emission. Contour levels are 3, 4, 5, 6.5, $8 \times \sigma_{\text{rms}}$, with $\sigma_{\text{rms}} = 4.5 \text{ mJy beam}^{-1} \text{ km s}^{-1}$. The blue arrow in (a) and the red arrow in (d) show the direction of the corresponding outflow lobes associated with ALMA1d. The dashed cyan line in (b) indicates the location of a dust lane structure. The velocity range of the moment maps is shown at the top of each frame, with zero systemic velocity equal to $v_{\text{LSR}} = -46.9 \text{ km s}^{-1}$. The locations of the continuum sources are marked with green crosses. The beam size is shown in the lower-left corner.

the error of the positions of the minima (see Appendix B). We obtain a separation between the minimum value of the Gaussians of 0.8 km s^{-1} and an error of 0.2 km s^{-1} . The $\text{CH}_3\text{CN } J_K = 12_3 - 11_3$ emission is likely tracing hotter gas than ^{13}CO (see Table 3); the shift indicates that the velocity of the infalling material is increasing toward the source (e.g., Beltrán et al. 2018, 2022). Additional observations with higher spectral resolution and/or better S/N are needed to separate these

features further, thus allowing a detailed study of the infall motion.

4. Discussion

Here we discuss the origin of the observed substructures, particularly the origin of the bow-shaped object. Its origin will be framed into two paradigms:

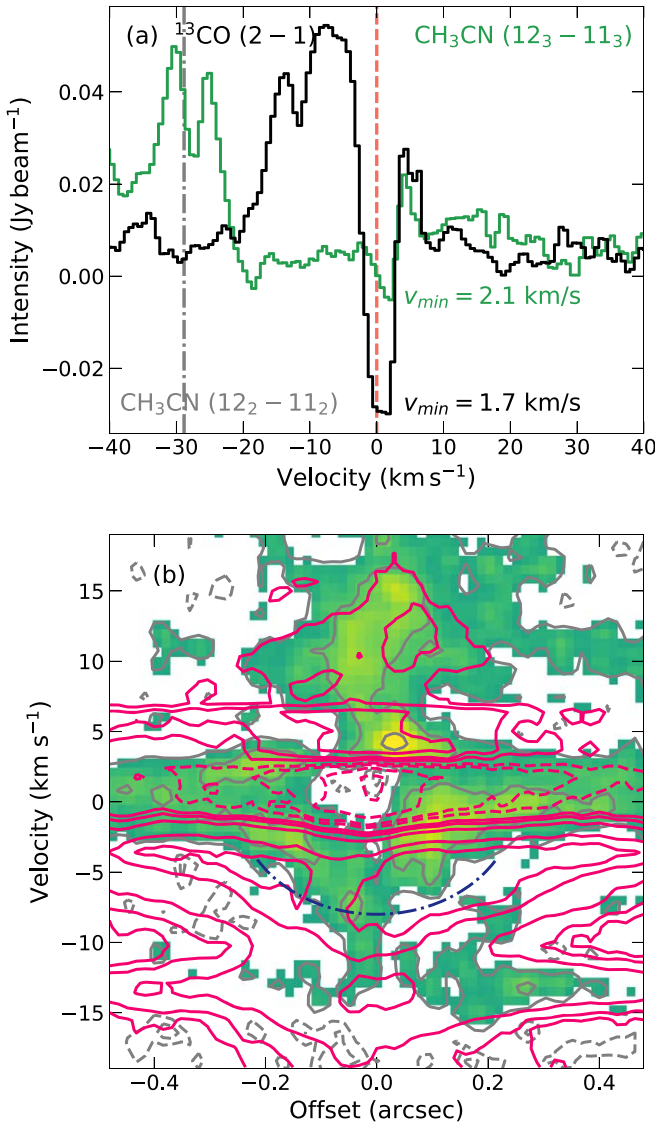


Figure 9. Infall profiles and *PV* maps toward ALMA1a. (a) CH₃CN $J_K = 12_3-11_3$ (green line) and ¹³CO $J = 2-1$ (black line) spectra toward ALMA1a. The vertical dashed red line marks the zero velocity and the vertical dotted-dashed gray line marks the position of the CH₃CN $J_K = 12_2-11_2$ transition. v_{\min} corresponds to the velocity at the minimum of the absorption. (b) *PV* maps of CH₃CN (color and gray contours) and ¹³CO (red contours). The CH₃CN contour levels are -4, -2, 4, 10, and 20 mJy beam⁻¹, while the ¹³CO contour levels are -30, -20, -10, -5, 5, 10, 20, 40, and 50 mJy beam⁻¹. The color map only shows the data values over 3σ with $\sigma = 1.2$ mJy beam⁻¹. The dotted-dashed line shows the “C” shape characteristic of infalling motions.

1. A shocked region of the outflow cavity.
2. A streamer feeding the central region and/or forming a third stellar component. The diagram in Figure 10 summarizes the findings of the previous section and the two aforementioned paradigms.

4.1. Outflow Origin

The location of the bow toward the southwest is consistent with the large-scale outflow direction (Figure 7(b)). Although the direction is not consistent with the bulk of the SiO emission (Figure 7(a)), the structure may be the result of the interaction of a wide-angle component of the outflow as indicated by the extended SiO emission in Figure 8(b). The interaction of the

outflow and the envelope material can produce an accumulation of gas resulting in the observed structure. Such structures are predicted by simulations (e.g., Kuiper et al. 2015; Kuiper & Hosokawa 2018) and have been observed in other high-mass star-forming regions (e.g., Preibisch et al. 2003).

The presence of unresolved free-free radio emission toward this region ($\sim 2''$ resolution; Avison et al. 2015) and in the observations presented here, where the continuum emission from different components can be separated, begs the question of whether the radio emission is produced by a jet rather than an HC H II region. We revisit the fit to the submillimeter/radio SED of Avison et al. (2015) to test whether the bow emission (red contour level in Figure 1) is produced by a jet. Here we assume that the free-free emission comes from ionized gas in the bow and fit a power law with a dust and a free-free component to the SED:

$$S_\nu = S_d \left(\frac{\nu}{\nu_0} \right)^{\beta+2} + S_{ff} \left(\frac{\nu}{\nu_0} \right)^\alpha, \quad (6)$$

where β is the dust emissivity index and α the free-free spectral index. Because we lack data at similar angular resolution at higher frequencies to fit the dust emissivity index, we assume $\beta = 1.97$ from Avison et al. (2015). Figure 5 shows the results of the fit. The fitted free-free spectral index of 1.5 is relatively insensitive to dust emissivity indices in the 1.5–2.0 range. This value is slightly smaller than that derived by Avison et al. (2015), $\alpha = 1.67-1.9$. A free-free spectral index of 1.5 is not common in jets (but plausible) and particularly not in shock ionized jets, where indices $\alpha < 0$ are expected (e.g., Purser et al. 2021).

The extended tentative H30 α emission is also not consistent with jet emission, which is more compact and closer to the source (e.g., Guzmán et al. 2020). The H30 α emission is more consistent with H II regions, but the extension of the emission would indicate that the source is more evolved than previously estimated by Avison et al. (2015, 2021).

4.2. Streamer Origin

Streamers feeding protostellar high-mass systems have been observed in a few other regions at 1000–10,000 au scales (e.g., Maud et al. 2017; Izquierdo et al. 2018b; Goddi et al. 2020; Sanhueza et al. 2021). The observations presented here show this type of structure at smaller scales (< 1000 au), which have been observed in disks of single systems (e.g., Maud et al. 2019; Johnston et al. 2020b). Simulations show that gravitational instabilities of the circumstellar disk can produce spiral-like arms that can feed the protostar in episodic bursts of accretion (e.g., Meyer et al. 2018; Mignon-Risse et al. 2021; Riaz et al. 2021). These simulations show overdensities with shapes similar to that of the continuum observations presented here and are predicted to be observable by ALMA at high resolution (Ahmadi et al. 2019; Meyer et al. 2019).

The stability of a spiral structure can be determined from the Hill criterion, which relates the self-gravity of the spiral structure to the shear forces exerted over it (Rogers & Wadsley 2012; Meyer et al. 2018). An unstable spiral would fragment and consequently form another star/planet, while a stable filament would continue to funnel gas to the disk interior (Rogers & Wadsley 2012). A spiral arm is unstable if the spiral width $l < 2R_{\text{Hill}}$ (Rogers & Wadsley 2012), with the Hill radius

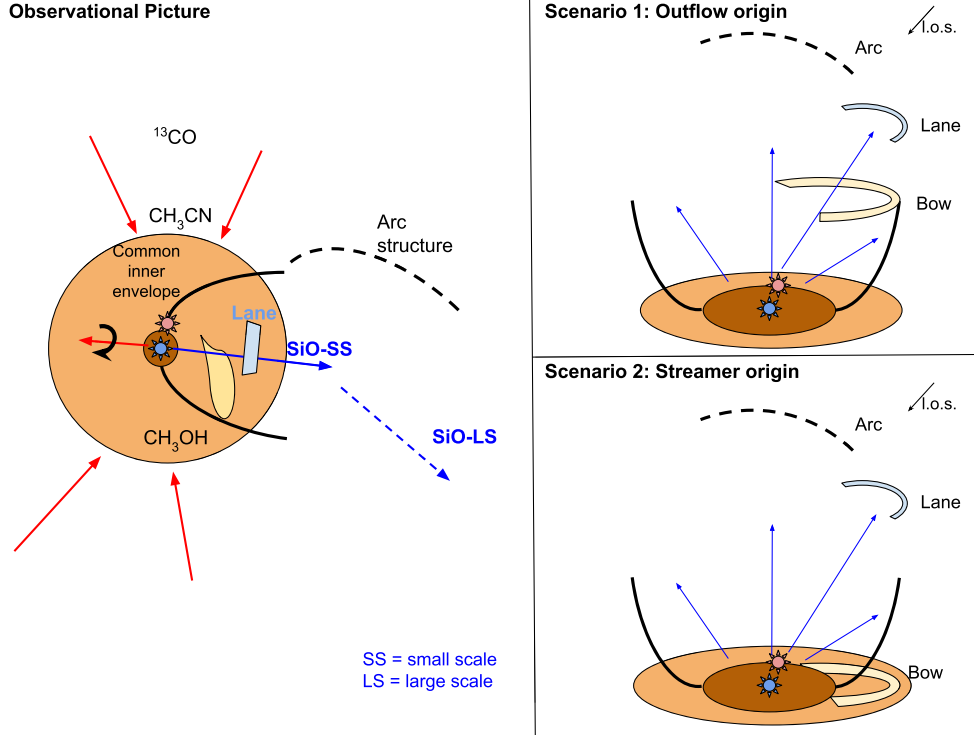


Figure 10. Diagram summarizing the findings of Section 3, and the discussion in Section 4 on the origin of the bow structure under an outflow origin and a streamer origin.

given by Rogers & Wadsley (2012),

$$R_{\text{Hill}} = \left(\frac{G\Sigma l^2}{3\Omega^2} \right)^{1/3}, \quad (7)$$

with Σ the surface density of the spiral, l the spiral width, and Ω the rotation rate. The surface density derived from the dust emission is $\Sigma = M_d/(\pi r^2) = 42 \text{ g cm}^{-2}$, while the bow width is $l = 0''.11 = 360 \text{ au}$. This width is measured across the 130σ level and passes through the peak emission in the radial direction with respect to ALMA1a. Width values range between $\sim 0''.02$ (65 au) up to $0''.14$ (455 au). From the rotation velocity v_ϕ , we obtain a rotation rate of $\Omega = |v_{\phi, \text{obs}}|/(r \sin i) = 1.0 \times 10^{-10} \text{ s}^{-1}$ for an inclination angle of 26° (see Section 3.4). This rotation rate is more than twice as high as those obtained in the line modeling presented in Paper I ($\lesssim 4 \times 10^{-11} \text{ s}^{-1}$). With these values, we obtain a Hill radius of $R_{\text{Hill}} = 92 \text{ au}$. This Hill radius implies that the spiral is stable. Governed by the gravity of the central sources, the spiral would be destined to be accreted by the binary system.

Figure 4(c) shows a velocity gradient along the spine of the bow structure with values ranging from $\sim 0.8 \text{ km s}^{-1}$ near the peak continuum emission to $\sim -0.3 \text{ km s}^{-1}$ closer to the binary sources. This velocity gradient, however, may be produced by the large-scale common disk rotation and/or contaminated by the outflow motion observed in the same direction. The lack of a velocity gradient in the bow structure from other molecular tracers due to weak line emission is the main caveat to confirm the streamer scenario. This is likely caused by the dust becoming optically thick at smaller scales (see Section 3.3). However, the presence of, e.g., C^{18}O absorption in Figure 2(f)

indicates that there is a temperature gradient which is not considered in the Hill criterion. This temperature gradient may be caused by an already-formed additional source or heating from the working surfaces of an accretion shock. On the other hand, under the outflow origin, the gradient can be produced by heating from the working surfaces of an outflow shock. In the cases of accretion and outflow shocks, the accumulation of gas would make the dust optically thick.

5. Conclusions

We analyzed high-resolution ALMA 1.3 mm observations of the high-mass source G335.579–0.272 MM1 ALMA1 that resolve scales of $\sim 200 \text{ au}$. The continuum observations reveal four sources inside the region, with ALMA1a and ALMA1b likely forming a binary system. We detect a fifth continuum peak located to the southwest of the binary system with a bow shape and connected to the main sources by continuum emission. These three sources are located at the center of the gravitational potential well of the ALMA1 region.

Line emission is damped toward the binary sources and the bow and appears in absorption in many common hot core lines (e.g., CH_3CN). These indicate that lines are becoming optically thick, and given the bright continuum, some are presenting inverse P Cygni profiles. Emission from CH_3OH transitions traces a common disk/inner envelope of $\sim 3000 \text{ au}$ diameter. Part of the emission is likely coming from gas in the blueshifted outflow cavity, where lines are wider. The surrounding emission shows a blueshifted central region surrounded by redshifted emission, characteristic of infalling matter when lines are becoming optically thick.

The lack of line emission tracing the kinematics of ALMA1b precludes the determination of the parameters from the binary system. Nonetheless, the CH_2CHCN emission tracing the gas

around ALMA1a allows us to determine its rotation direction and estimate a Keplerian mass of $3 M_{\odot}$ under an estimated inclination angle of the system of 26° . This inclination estimate is based on geometrical considerations of the shape of the CH_2CHCN emission and is smaller than previous estimates from outflows, which indicate the precession of the sources.

ALMA1a is powering the outflow as shown by SiO emission. The direction of the outflow close to the source is consistent with the rotation axis as derived from the CH_2CHCN velocity gradient (P.A. = 240°). SiO features are consistent with features in the continuum, indicating the location of previous interactions between the outflow and the envelope cavity walls.

We explore the origin of the bow. While its location and outflow line emission support an outflow origin for the structure as matter is swept and/or shocked along the outflow cavity walls, there is not enough evidence to discard an infalling streaming origin. The latter could be accreted by the central source(s) in burst or even form a third companion. Additional multiwavelength observations at similar resolutions are necessary to assess the bow origin.

The authors would like to thank the anonymous referee for the thoughtful feedback. F.O. and H.-R.V.C. acknowledge the support of the Ministry of Science and Technology of Taiwan, projects No. 109-2112-M-007-008-, 110-2112-M-007-023-, and 110-2112-M-007-034-. P.S. was partially supported by a Grant-in-Aid for Scientific Research (KAKENHI Number 18H01259) of the Japan Society for the Promotion of Science (JSPS). A.G. acknowledges support from NSF grant AST 2008101. This paper makes use of the following ALMA data: ADS/JAO.ALMA#2016.1.01036.S. ALMA is a partnership of ESO (representing its member states), NSF (USA) and NINS (Japan), together with NRC (Canada), MOST and ASIAA (Taiwan), and KASI (Republic of Korea), in cooperation with the Republic of Chile. The Joint ALMA Observatory is operated by ESO, AUI/NRAO and NAOJ.

Facility: ALMA.

Software: CASA (McMullin et al. 2007), astropy (Astropy Collaboration et al. 2013; Price-Whelan et al. 2018), GoContinuum (Olguin & Sanhueza 2020), YCLEAN (Contreras 2018), CASSIS (Vastel et al. 2015).

Appendix A Additional Figures

Figure 11 presents moment maps of tentative $\text{H}30\alpha$ emission toward G335 ALMA1. Figure 12 presents error maps from the

LTE fitting to CH_3OH spectra for the physical properties presented in Figure 4, while Figure 13 show the fitted spectra toward the continuum peak positions of ALMA1a, ALMA1b and the bow structure. Figure 14 shows the location of ALMA1a and ALMA1b with respect to the larger ALMA1 region presented in Paper I. Figure 15 presents the PV map of the CH_2CHCN emission along the velocity gradient direction (P.A. = 150°) in ALMA1a.

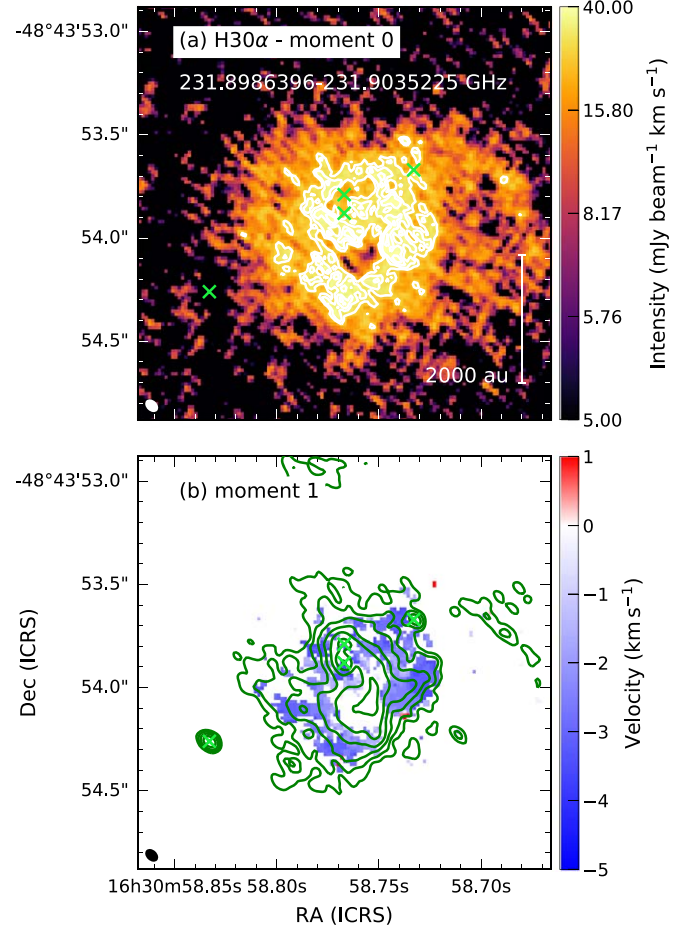


Figure 11. Tentative $\text{H}30\alpha$ emission in G335 ALMA1. (a) Zeroth-order moment map. Contour levels are 5, 6, 7, $8 \times \sigma_{\text{rms}}$, with $\sigma_{\text{rms}} = 5.4 \text{ mJy beam}^{-1} \text{ km s}^{-1}$. The frequency range shown in the figure corresponds to the frequency integration range in the rest frame. (b) First-moment map in color scale. Zero systemic velocity corresponds to the source $v_{\text{LSR}} (-46.9 \text{ km s}^{-1})$. Contours correspond to the continuum emission (see Figure 1b). The beam is shown in the lower-left corner.

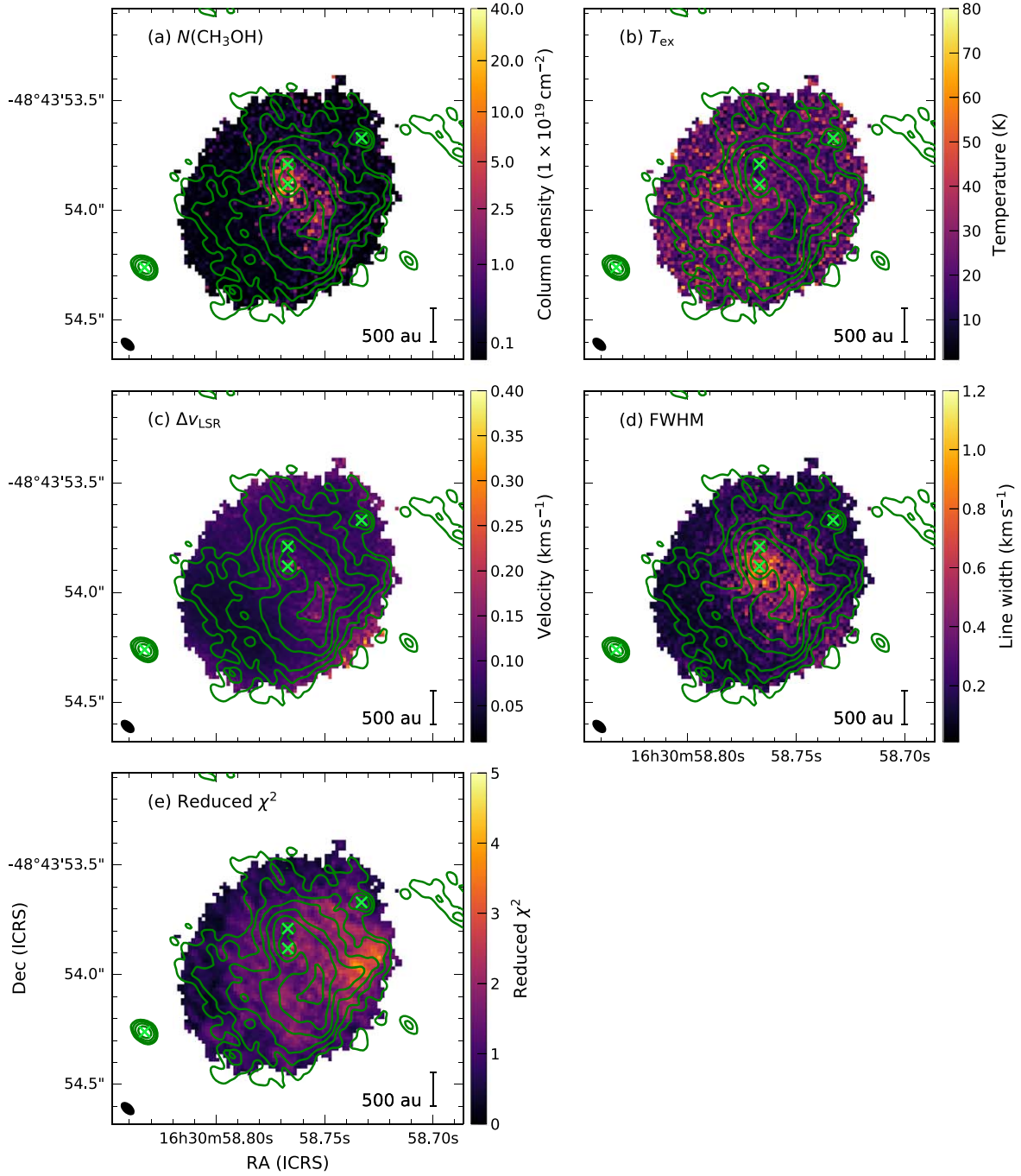


Figure 12. CH₃OH LTE modeling standard deviation maps and reduced- χ^2 map. (a) CH₃OH column density error map. (b) Excitation temperature error map. (c) Velocity shift with respect to the systemic velocity error map. (d) Line FWHM error map. (e) χ^2 map contour levels correspond to $5, 8, 12, 16, 20 \times \sigma_{\text{rms}}$, with $\sigma_{\text{rms}} = 11 \text{ mJy beam}^{-1}$. The green contours correspond to the continuum emission from the extended configuration, Figure 1(b). The location of the continuum sources is marked with green crosses. The beam size is shown in the lower-left corner.

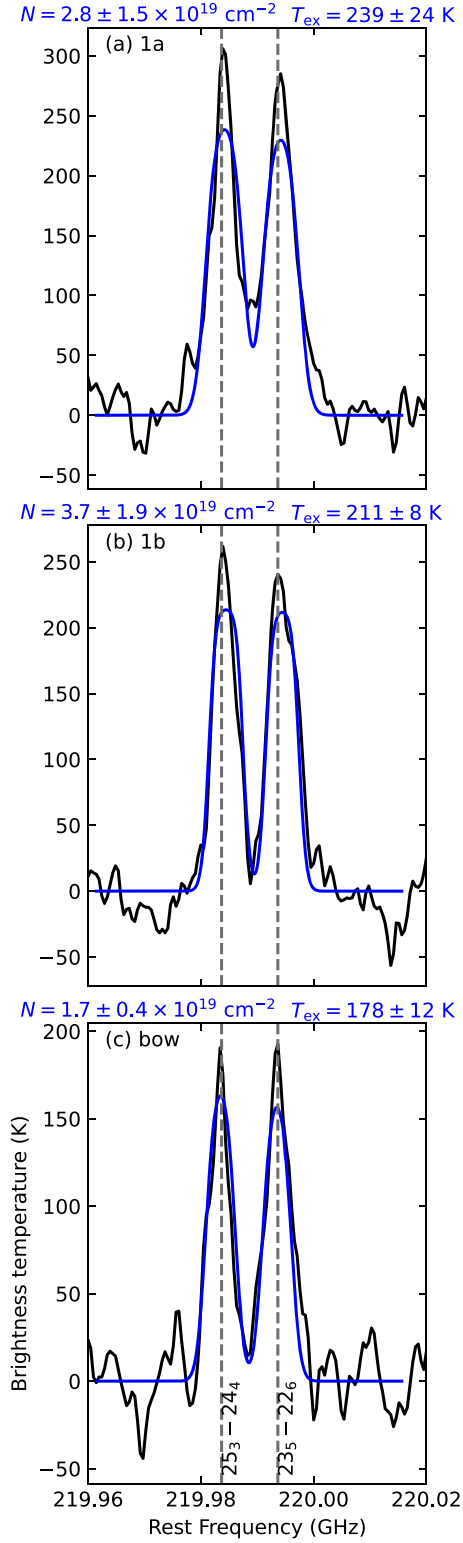


Figure 13. CH_3OH line emission toward the continuum peak of (a) ALMA1a, (b) ALMA1b, and (c) the bow structure. Observations are presented in black lines, while the best-fitting model is shown in blue lines. The column density, N , and excitation temperature, T_{ex} , of the best-fitting model and 1σ errors are shown over each panel. Vertical dashed lines correspond to the transition frequency.

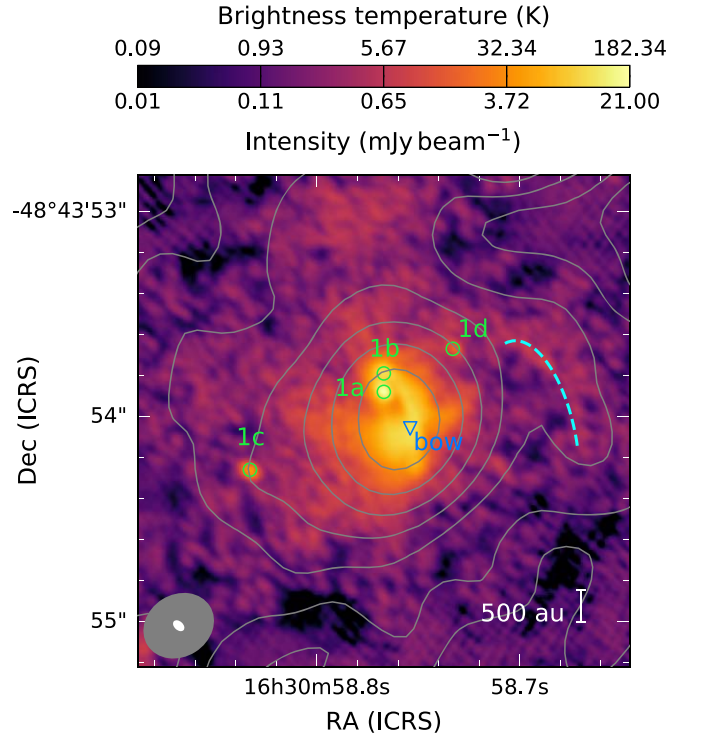


Figure 14. Continuum maps of ALMA1 from the combined configuration (color scale) and compact configuration from Paper I (gray contours). Contour levels are 5, 10, 20, 40, 80, 160, and $320 \times \sigma_{\text{cont}}$, with $\sigma_{\text{cont}} = 0.4 \text{ mJy beam}^{-1}$ and a beam size of $0''.36 \times 0''.30$. Continuum sources are marked with green circles. The dashed line shows the arc-like structure detected in the compact configuration data. The beam of the compact configuration is shown in the lower-left corner in gray while the beam of the combined configuration is shown in white.

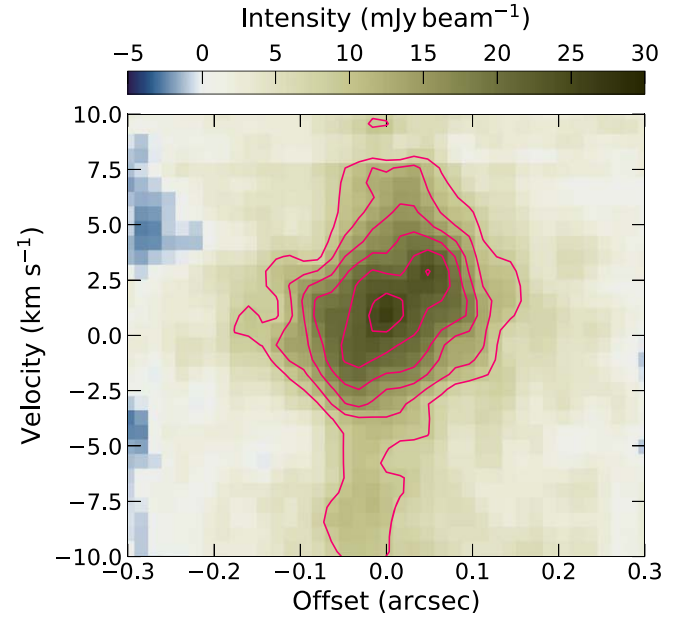


Figure 15. Position-velocity map of CH_2CHCN emission from the combined data set. Contour levels are 3, 4, ... $8 \times \sigma$ with $\sigma = 3 \text{ mJy beam}^{-1}$. The map was calculated in a slit centered in the position of ALMA1a with P. A. = 150° and width of $0''.05$.

Appendix B

Inverse P Cygni Gaussian Fit

In order to estimate the statistical significance of the distance between the minima of the inverse P Cygni of CH₃CN and ¹³CO, we first fit a Gaussian to the intensity of the form:

$$I(v) = B - A \exp\left(-\frac{(v - \mu)^2}{2\sigma^2}\right). \quad (\text{B1})$$

We limit the fit to the points in the absorption profile and fix the baseline, B . Figure 16 shows these fitted data and the values of the best fit.

To estimate the error in the value of the velocity at the minimum, μ , we adapt the expected position uncertainty equation for astrometric measurements in Reid et al. (1988), as

$$\sigma_\mu = \left(\frac{4}{\pi}\right)^{0.25} \frac{\sigma_{\text{rms}}}{A} \sigma, \quad (\text{B2})$$

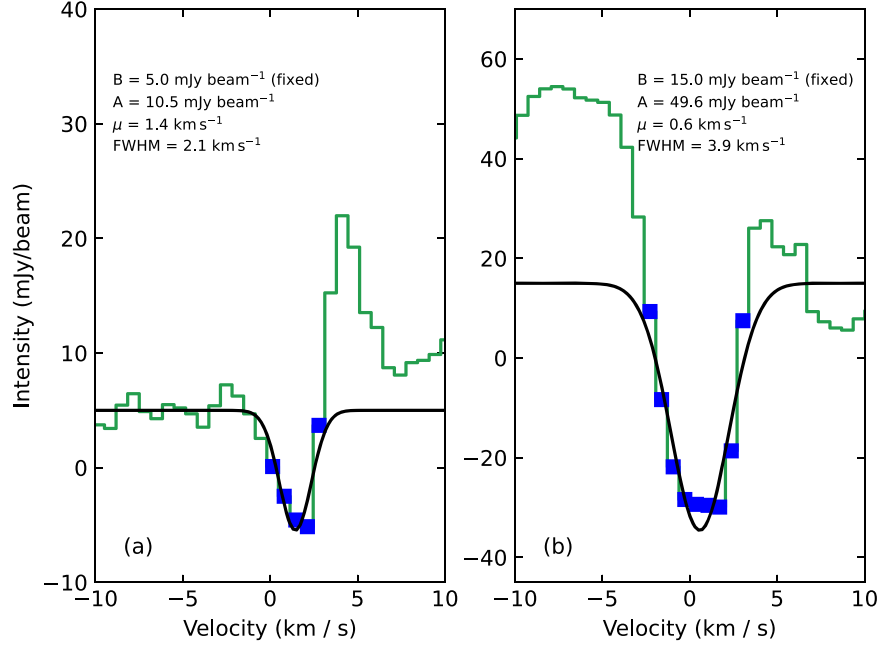



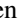






Figure 16. Gaussian fit to the inverse P Cygni profile of (a) CH₃CN $J=12-11$ $K=3$ and (b) ¹³CO $J=2-1$ toward G335 ALMA1a. The green line shows the data in Figure 9, blue squares correspond to the fitted points, and the black line shows the fit.

with $\sigma_{\text{rms}} = 2 \text{ mJy beam}^{-1}$ the noise per channel. We obtain $\sigma_{\mu} = 0.2$ and 0.1 km s^{-1} for CH_3CN and ^{13}CO , respectively.

ORCID iDs

Fernando A. Olguin  <https://orcid.org/0000-0002-8250-6827>
 Patricio Sanhueza  <https://orcid.org/0000-0002-7125-7685>
 Adam Ginsburg  <https://orcid.org/0000-0001-6431-9633>
 Huei-Ru Vivien Chen  <https://orcid.org/0000-0002-9774-1846>
 Qizhou Zhang  <https://orcid.org/0000-0003-2384-6589>
 Shanghuo Li  <https://orcid.org/0000-0003-1275-5251>
 Xing Lu  <https://orcid.org/0000-0003-2619-9305>
 Takeshi Sakai  <https://orcid.org/0000-0003-4521-7492>

References

- Ahmadi, A., Kuiper, R., & Beuther, H. 2019, *A&A*, **632**, A50
- Astropy Collaboration, Robitaille, T. P., Tollerud, E. J., et al. 2013, *A&A*, **558**, A33
- Avison, A., Fuller, G. A., Peretto, N., et al. 2021, *A&A*, **645**, A142
- Avison, A., Peretto, N., Fuller, G. A., et al. 2015, *A&A*, **577**, A30
- Belloche, A., Müller, H. S. P., Menten, K. M., Schilke, P., & Comito, C. 2013, *A&A*, **559**, A47
- Beltrán, M. T., Cesaroni, R., Rivilla, V. M., et al. 2018, *A&A*, **615**, A141
- Beltrán, M. T., Rivilla, V. M., Cesaroni, R., et al. 2022, *A&A*, **659**, A81
- Contreras, Y. 2018, Automatic Line Clean, v1.0, Zenodo, doi:10.5281/zenodo.1216881
- Contreras, Y., Sanhueza, P., Jackson, J. M., et al. 2018, *ApJ*, **861**, 14
- Crockett, N. R., Bergin, E. A., Neill, J. L., et al. 2014, *ApJ*, **787**, 112
- Estalella, R., Anglada, G., Díaz-Rodríguez, A. K., & Mayen-Gijón, J. M. 2019, *A&A*, **626**, A84
- Goddi, C., Ginsburg, A., Maud, L. T., Zhang, Q., & Zapata, L. A. 2020, *ApJ*, **905**, 25
- Guzmán, A. E., Sanhueza, P., Zapata, L., Garay, G., & Rodríguez, L. F. 2020, *ApJ*, **904**, 77
- Hosokawa, T., Yorke, H. W., & Omukai, K. 2010, *ApJ*, **721**, 478
- Izquierdo, A. F., Galván-Madrid, R., Maud, L. T., et al. 2018a, *MNRAS*, **478**, 2505
- Izquierdo, A. F., Galván-Madrid, R., Maud, L. T., et al. 2018b, *MNRAS*, **478**, 2505
- Johnston, K. G., Hoare, M. G., Beuther, H., et al. 2020a, *ApJ*, **896**, 35
- Johnston, K. G., Hoare, M. G., Beuther, H., et al. 2020b, *A&A*, **634**, L11
- Kauffmann, J., Bertoldi, F., Bourke, T. L., Evans, N. J. I., & Lee, C. W. 2008, *A&A*, **487**, 993
- Krumholz, M. R., Klein, R. I., & McKee, C. F. 2007, *ApJ*, **656**, 959
- Krumholz, M. R., Klein, R. I., & McKee, C. F. 2012, *ApJ*, **754**, 71
- Kuiper, R., & Hosokawa, T. 2018, *A&A*, **616**, A101
- Kuiper, R., Yorke, H. W., & Turner, N. J. 2015, *ApJ*, **800**, 86
- Lizano, S. 2008, in ASP Conf. Ser. 387, Massive Star Formation: Observations Confront Theory, ed. H. Beuther, H. Linz, & T. Henning (San Francisco, CA: ASP), 232
- López, A., Tercero, B., Kisiel, Z., et al. 2014, *A&A*, **572**, A44
- Maud, L. T., Cesaroni, R., Kumar, M. S. N., et al. 2019, *A&A*, **627**, L6
- Maud, L. T., Hoare, M. G., Galván-Madrid, R., et al. 2017, *MNRAS*, **467**, L120
- McMullin, J. P., Waters, B., Schiebel, D., Young, W., & Golap, K. 2007, in ASP Conf. Ser. 376, Astronomical Data Analysis Software and Systems XVI, ed. R. A. Shaw, F. Hill, & D. J. Bell (San Francisco, CA: ASP), 127
- Menten, K. M., Walmsley, C. M., Henkel, C., & Wilson, T. L. 1986, *A&A*, **157**, 318
- Meyer, D. M. A., Kreplin, A., Kraus, S., et al. 2019, *MNRAS*, **487**, 4473
- Meyer, D. M. A., Kuiper, R., Kley, W., Johnston, K. G., & Vorobyov, E. 2018, *MNRAS*, **473**, 3615
- Mignon-Risse, R., González, M., Commerçon, B., & Rosdahl, J. 2021, *A&A*, **652**, A69
- Müller, H. S. P., Schlöder, F., Stutzki, J., & Winnewisser, G. 2005, *JMoSt*, **742**, 215
- Olguin, F., & Sanhueza, P. 2020, Gocontinuum: continuum finding tool, v2.0.0, Zenodo, doi:10.5281/zenodo.4302846
- Olguin, F. A., Hoare, M. G., Johnston, K. G., et al. 2020, *MNRAS*, **498**, 4721
- Olguin, F. A., Sanhueza, P., Guzmán, A. E., et al. 2021, *ApJ*, **909**, 199
- Ossenkopf, V., & Henning, T. 1994, *A&A*, **291**, 943
- Peretto, N., Fuller, G. A., Duarte-Cabral, A., et al. 2013, *A&A*, **555**, A112
- Pickett, H. M., Poynter, R. L., Cohen, E. A., et al. 1998, *JQRST*, **60**, 883
- Preibisch, T., Balega, Y. Y., Schertl, D., & Weigelt, G. 2003, *A&A*, **412**, 735
- Price-Whelan, A. M., Sipőcz, B. M., Günther, H. M., et al. 2018, *AJ*, **156**, 123
- Purser, S. J. D., Lumsden, S. L., Hoare, M. G., & Kurtz, S. 2021, *MNRAS*, **504**, 338
- Reid, M. J., Schneps, M. H., Moran, J. M., et al. 1988, *ApJ*, **330**, 809
- Riaz, R., Schleicher, D. R. G., Vanaverbeke, S., & Klessen, R. S. 2021, *MNRAS*, **507**, 6061
- Rogers, P. D., & Wadsley, J. 2012, *MNRAS*, **423**, 1896
- Sanhueza, P., Contreras, Y., Wu, B., et al. 2019, *ApJ*, **886**, 102
- Sanhueza, P., Girart, J. M., Padovani, M., et al. 2021, *ApJL*, **915**, L10
- Sanhueza, P., Jackson, J. M., Zhang, Q., et al. 2017, *ApJ*, **841**, 97
- Smith, R. J., Longmore, S., & Bonnell, I. 2009, *MNRAS*, **400**, 1775
- Stephens, I. W., Jackson, J. M., Sanhueza, P., et al. 2015, *ApJ*, **802**, 6
- Tanaka, K. E. I., Zhang, Y., Hirota, T., et al. 2020, *ApJL*, **900**, L2
- Vastel, C., Bottinelli, S., Caux, E., Glorian, J. M., & Boiziot, M. 2015, in SF2A-2015: Proceedings of the Annual meeting of the French Society of Astronomy and Astrophysics (Paris: SAF), 313
- Vázquez-Semadeni, E., Palau, A., Ballesteros-Paredes, J., Gómez, G. C., & Zamora-Avilés, M. 2019, *MNRAS*, **490**, 3061
- Zhang, Q., & Ho, P. T. P. 1997, *ApJ*, **488**, 241
- Zhang, Y., Tan, J. C., Tanaka, K. E. I., et al. 2019, *NatAs*, **3**, 517